Research Square

Preprints are preliminary reports that have not undergone peer review.
They should not be considered conclusive, used to inform clinical practice,
or referenced by the media as validated information.

Chemically and Microstructurally Modulated High-Temperature Release of CsI in Nd-doped UO2 Nanoceramics

Gabriel Murphy

g.murphy@fz-juelich.de

Forschungszentrum Juelich GmbH https://orcid.org/0000-0003-3239-9725

Daniil Shirokiy

Marco Cologna

European Commission

Felix Brandt

Jean-Yves Colle

Damien Prieur

Helmholtz-Zentrum Dresden-Rossendorf https://orcid.org/0000-0001-5087-0133

Olaf Walter

Walter Bonani

European Commission

Anna Isabel Martinez Ferri

Ondřej Benes

Martina Klinkenberg

Răzvan Buda

Dirk Bosbach

https://orcid.org/0000-0002-6099-0400

Karin Popa

European Commission, Joint Research Centre Karlsruhe (JRC) https://orcid.org/0000-0003-2759-6492

Article

Keywords: Oxide Fuel, High Burn-Up Structure, Fission Product Release, Speciation, Neodymium

Posted Date: September 1st, 2026

DOI: https://doi.org/10.21203/rs.3.rs-10275945/v1

License: This work is licensed under a Creative Commons Attribution 4.0 International License.
Read Full License

Additional Declarations: There is **NO** Competing Interest.

Version of Record: A version of this preprint was published at Communications Materials on October 30th, 2026. See the published version at https://doi.org/10.1038/s43246-026-01411-7.

Manuscript

Chemically and Microstructurally Modulated High-Temperature Release of CsI in Nd-doped UO_2 Nanoceramics

Daniil Shirokiy[1*], Karin Popa[2*], Marco Cologna[2], Felix Brandt[1], Jean-Yves Colle[2], Damien Prieur[3,4], Olaf Walter[2], Walter Bonani[2], Anna Isabel Martinez Ferri[2], Ondřej Beneš[2], Martina Klinkenberg[1], Răzvan Buda[2], Dirk Bosbach[1] and Gabriel L. Murphy[1*]

[1]*Institute of Fusion Energy and Nuclear Waste Management (IFN-2), Forschungszentrum Jülich GmbH, 52428 Jülich, Germany*

[2]*European Commission, Joint Research Centre (JRC), Karlsruhe, Germany*

[3]*Rossendorf Beamline (BM20), European Synchrotron Radiation Facility, Avenue des Martyrs 71, 38043 Grenoble, France*

[4]*Institute of Resource Ecology, Helmholtz-Zentrum Dresden-Rossendorf, Bautzner Landstraße 400, 01328 Dresden, Germany*

** Corresponding authors: Daniil Shirokiy (d.shirokiy@fz-juelich.de) , Karin Popa (karin.popa@ec.europa.eu), Gabriel L. Murphy (g.murphy@fz-juelich.de)*

Abstract

The unexpected discharge of instant release fraction elements, such as Cs and I, from irradiated nuclear fuel, is one of the most concerning scenarios that may occur during in-pile irradiation, subsequent storage and final disposal, yet the underlying chemistry behind its release is poorly understood. Herein, we have examined the speciation of CsI within UO_2 nanoceramics doped with Nd as a proxy for high burn-up fuel synthesised via spark plasma sintering. We demonstrate via X-ray absorption spectroscopy and electron microscopy that the addition of Nd impacts the chemical speciation and dissociation of CsI in the examined materials. High temperature release studies using Knudsen effusion mass spectrometry reveal varying release patterns corresponding to Nd addition. The results of this investigation indicate that the chemistry of the UO_2 high burn-up fuel matrix, its specific microstructure and associated soluble fission products, impact the high temperature release of Cs and I within irradiated fuel.

Key words:

Oxide Fuel, High Burn-Up Structure, Fission Product Release, Speciation, Neodymium

1. Introduction

In the pursuit of reducing the volume of spent nuclear fuel (SNF) and increasing energy production efficiency, there is an increasing demand for more efficient, higher burn-up nuclear fuels which has subsequently created popular attention.[1-4] Increased fuel burn-up results in a correspondingly higher content of fission products (FPs), whereas when the local burn-up of typical nuclear UO_2 fuel exceeds 55 GWd/tHM, microstructural changes occur, and what is known as the "high burn-up structure" (HBS) emerges.[5-7] The HBS comprises nanograins measuring ~100 – 300 nm,[7] and is characterised by an increased content of FPs and higher porosity, caused by the development of fission gas pores.[5,8] These structures are often observed at the periphery of SNF pellet, where temperatures are lower while thermal neutrons flux and accordingly burn-up are typically higher; hence, they are also referred to as "rim structures".[7,9] The mechanism underlying the formation of HBS may result from the emergence and growth of fission gas bubbles, followed by the formation of small subgrains from the original grains.[5,10] Interest in the study of HBS is attracted by its ability to influence the mechanical properties and swelling of fuel, as well as the release of gaseous and volatile FPs during irradiation in reactor,[11] or during an unexpected fuel breach event. What is known as the instant release fraction (IRF) is considered one of the most concerning of these release processes as it can readily compromise the integrity and safety of irradiated fuel when in reactor, storage or within a repository. The IRF is defined as the proportion of FPs radionuclides that are not chemically bound in the UO_2 fuel matrix and can be rapidly released from fuel or fuel assemblies in the event of containment breach,[12,13] (for example, due to mechanical impact, corrosion or meltdown) or subsequent contact with water.[14,15] Consequently, understanding the role of the HBS in influencing the release of the IRF is critical for both safe usage and final disposal of high burn-up fuels.

The instantaneous release of radionuclides from irradiated nuclear fuel following a breach event is understood to occur through two mechanisms: from the gap (that includes fuel-

cladding gap and fractures), and from grain boundaries, whereas in the case of a meltdown, a matrix diffusion mechanism is also involved.[11,13,16] Elements in the IRF include a series of radioisotopes, with particular attention given here to the radioactive isotopes of iodine (I) and caesium (Cs), including ^{129}I ($T_{1/2}$ = 1.57·10^7 y), ^{135}Cs ($T_{1/2}$ = 2.3·10^6 y) and ^{137}Cs ($T_{1/2}$ = 30.08 y). Both elements, Cs and I, belong to the volatile and gaseous FPs group, but Cs also classifies as a FP that form oxide precipitates.[13,17-19] As the IRF-related elements, Cs and I are typically found in both the fuel-cladding gap and grain boundary regions.[14] Despite thermodynamic calculations predicting the favourability of CsI compound formation in reactor conditions,[20] CsI has not often observed in SNF.[21,22] This has been proposed to be in-part due to γ-induced radiolysis.[22,23] The behaviour and release of Cs and I from irradiated fuel has been studied using numerous methods, such as leaching experiments[11,24-26] and high-temperature methods,[27] particularly via Knudsen effusion mass spectrometry (KEMS).[28-32] Experiments that were focusing on high burn-up SNF showed that the release of IRF-related radionuclides from HBS regions differs from the release from the non-HBS regions of SNF, even when considering differences in FPs inventories.[11,24,31] Consequently, the emergent roles of FP content and the structural-chemical nature of HBS in dictating behaviour and release of IRF-related radionuclides remains unclear.

Precisely investigating effects pertaining to IRF release from the HBS of irradiated fuel are often achieved via model system methods. Model systems are used to study the individual effects of SNF while excluding their mutual influence and avoiding the dangers associated with the high radioactivity of actual SNF samples.[33-37] However, they often involve the use of high-temperature stages, such as conventional sintering of UO_2, which typically reach temperatures above 1600°C.[33] Long sintering at such temperatures are above the CsI boiling point (1280°C) and will lead to its complete evaporation, which imposes limitations on the study of the behaviour and chemistry of Cs and I species using CsI-doped UO_2 model systems. Moreover, these sintering conditions lead to significant grain growth,[38] which hinders the synthesis of ceramics with grain sizes comparable to the HBS. As an alternative to high-

temperature sintering, spark plasma sintering (SPS) allows to sinter materials at lower temperatures and for shorter periods of time, thereby avoiding both complete evaporation of CsI and undesirable grain growth. It is therefore better suited to ensure the incorporation of Cs and I into the nanograined structure of sintered UO_2, enabling the subsequent examination of the associated microstructural effects and release towards the real HBS.[39]

Previous studies of CsI-doped UO_2 model materials, and their comparison against actual SNF using KEMS revealed different Cs and I release temperatures for each group of samples within the measured ranges, as well as different signal shapes.[22,29,31,32] This suggests that the current model system investigations performed do not completely account for all physical or chemical aspects occurring in actual SNF, promoting the need for more encompassing separate effect studies. The retention of Cs and I up to the temperatures of UO_2 matrix evaporation and their release rates may be influenced by factors such as the microstructure of UO_2, oxygen stoichiometry, radiation fields and the presence of FPs. Pertinently, the role of soluble in fuel matrix minor actinides and FPs, such as lanthanides, in the release of Cs and I has not been examined in model material investigations, nor within microstructures that consistent with the HBS. Although the IRF-related elements including Cs and I are understood to not incorporate within the UO_2 fuel matrix, van der Waals force between Cs and I species with the UO_2 matrix can be expected to change with incorporation of soluble FPs due to changes in redox chemistry. This includes the aliovalent substitution of U^{4+} with Nd^{3+}, resulting in the oxidation of U^{4+} to U^{5+}.[37,40] Nevertheless, it remains an open question as to whether matrix-soluble FPs, which occur at higher quantities in higher burn-up fuels, play a significant role in the behaviour and release of IRF elements such as Cs and I, consequently demanding such investigation.

Considering the pertinence of IRF in higher burn-up fuels potentially occurring during accident scenarios at reactor and repository facilities, it is paramount to determine underlying chemical physics, particularly that of the HBS. This study has consequently examined CsI-incorporated UO_2 model nanoceramic materials with varying levels of Nd as a soluble in matrix FP proxy in

order to bridge the gap between single-effect studies and those of irradiated fuel in order to identify key factors contributing to Cs and I chemistry and release. This is achieved through a thorough analysis of the chemistry and behaviour of Cs and I in nanostructured UO_2 mimicking the HBS in the presence of FP soluble in the UO_2 matrix, including their temperature-induced release. In the present work, neodymium (Nd) was used, since it is known to be an inactive surrogate for minor actinides, such as americium and curium, due to the closest matching ionic radii,[41,42] and is also highly relevant to the HBS since its local concentration increases linearly with fuel burn-up.[5] The study subsequently examines the CsI-included Nd-doped nanostructured UO_2 systematically by varying the levels of Nd from 0, 15 to 30 mol %, which, although it exceeds the amount of minor actinides and Nd in HBS itself,[5,17,43] it allows to reliably probe the influence of Nd presence independently from the other factors, as it provides a greater magnitude of effect upon the material's chemical properties. To incorporate Cs and I into the UO_2 structure, SPS was used with sintering conditions, determined during SPS optimisation cycles, to synthesise a variable mixture of Nd-doped UO_2 nanopowder with controlled amount of CsI powders. The obtained materials were investigated for their microstructural and chemical surface speciation, bulk chemistry and redox in addition to release mechanisms by energy dispersive X-ray (EDX) spectroscopy, X-ray absorption near edge structure (XANES), and KEMS analysis respectively. The results obtained are discussed in the context of the current understanding of the release of IRF-related Cs/I from the HBS of irradiated fuel with a high burn-up, and the influence of structural chemistry and the inventory of FPs.

2. Methods

2.1. Materials and synthesis

A hydrothermal decomposition method, derived from a previously reported one,[44] was used for the synthesis of UO_2 and Nd-doped UO_2 nanopowder precursor material. A $Nd(NO_3)_3 \cdot 6H_2O$ solution, produced by dissolving Nd_2O_3 (Alfa Aesar, 99.9%) in nitric acid, was mixed with a

$UO_2(NO_3)_2 \cdot 6H_2O$ solution stoichiometrically for targeted final $(U_{1-y}Nd_y)O_2$ compositions of y = 0, 15 and mol 30%. To these solutions, hydrazinium hydroxide N_2H_5OH (Sigma-Aldrich, about 100%) was added triggering a rapid precipitation consistent with literature.[44] The mixtures were placed in a 100 ml autoclave (model 4793, *p-T* controlled, Parr Instruments Company, USA) with a Teflon inset, where deionised water was added so that the remaining free volume was 35 ml and the pH of the final mixtures was found to be ~9.5 in all samples. The hermetically sealed mixtures were then heated to 180°C and held at this constant temperature for five hours, after which the mixture was cooled to room temperature at a rate of ~2.5°C/min. The peak excess pressure was in range of 20 – 30 bar. The resulting suspension was dried at room temperature until the liquid had completely evaporated, after which all samples were reduced in an atmosphere of Ar/6.5% H_2 ~1 l/min in a furnace, that was heated to a temperature of 500°C at a rate of 100°C/h, held for 4 hours, and then cooled to room temperature at a rate of 200°C/h. The samples were then manually mixed with CsI powder (Suprapure®, Merck) at a concentration of 3% mol in a mortar in a glove box.

2.2. Spark plasma sintering

$(U_{1-y}Nd_y)O_2$–(CsI) powder mixtures were placed in portions of ~300 mg in a graphite die, pre-pressed at 17.7 MPa and loaded into a SPS furnace (FCT Systeme GmbH, Rauenstein, Germany) installed in a glove box.[45] As the final microstructure of the samples, as well as CsI evaporation, are affected by the SPS sintering temperature and dwell time, several optimisation runs were performed to select suitable SPS parameters in order to ensure comparability between examined samples. These are discussed in later sections of this investigation. The sintered test samples were examined using scanning electron microscopy (SEM, details in the respective section) to verify the grain size and the homogeneity of the CsI particles distribution. The following optimised SPS parameters were selected the synthesis of subsequently investigated materials: heating in an argon atmosphere at a rate of 100°C/min to 950°C under a uniaxial pressure of 70.7 MPa, a dwell time of 5 s, cooling to 400°C at a rate

of 200°C/min and, after reducing the pressure to 17.7 MPa, followed by cooling down to room temperature with any heating removed (free cooling). Sintered ceramic specimens were recovered for subsequent analysis. The molar concentration of elements in the sintered samples was determined and verified using inductively coupled plasma mass spectrometry, ICP-MS (Thermo Element2, Thermo Electron Corporation, Germany), using developed methodology.[46]

2.3. Variable temperature X-ray powder diffraction

To confirm the phase composition, probe for chemical decomposition and structural changes at elevated temperatures, variable temperature X-ray powder diffraction (VT-XRD) was performed using a Bruker D8 Advance diffractometer with Bragg–Brentano (θ/2θ) geometry, equipped with a Kα1 monochromator and a Lynxeye detector. During the measurements a vacuum atmosphere was used. Diffractograms were collected for each sample that were mounted on platinum (Pt) holders at an ambient temperature of 30°C, followed by heating at the following temperature steps: 100, 300, 500, 700, 900 and 1150°C. The data were collected in the 2θ range of 20 – 120°, and the diffractograms were analysed in the 2θ range of 20 – 70° using the Rietveld method as implemented in GSAS-II software.[47]

2.4. Electron Microscopy

The microstructure of the samples produced and trialled during the SPS parameter optimisation and initial microstructure examination, as well as the inspection of unsintered powders, were performed with SEM using a VEGA electron microscope (Tescan, Czech Republic) equipped with an Everhart-Thornley Detector (ETD) at 30 kV. The morphology of the sintered pellets was examined using an Apreo 2 C LoVac electron microscope (ThermoFisher Scientific, Netherlands), which was also used for EDX mapping (Octane elect PLUS Silicon Drift Detector, EDAX, Weiterstadt, Germany) at 20 kV. For this purpose, pellet fragments with relatively flat pellet cross-section surfaces were selected. EDX maps were collected with an accelerating voltage of 20 kV for the edges: C K-edge, O K-edge, I L-edge,

Cs L-edge, Nd L-edge, and U M-edge. Additionally, spot EDX measurements were performed to analyse various microparticles and impurities found on the unpolished cross-sectional surface.

2.5. X-ray absorption spectroscopy near edge structure

XANES measurements on the Cs and I K-edges were performed at the ROBL[48] beamline at the ESRF in Grenoble, France. The incident energy was scanned using a water-cooled Si(111) double monochromator around the corresponding edge. Two Pt mirrors, positioned before and after the monochromator, were used to collimate the beam, reject higher harmonics, and focus it on the sample. Prior to measurement, the samples were ground into a powder, mixed with boron nitride at a weight ratio of 1:10, and then pressed into pellets. The spectra were collected at ambient temperature using an 18-element solid-state germanium detector (Ultra-LEGe, GUL0055, Mirion Technologies) The detector was tuned to the maximum intensity of the emission line of the corresponding in non-resonant mode (incident energy above the corresponding edge). All measurements were performed at 25°C.

2.6. Knudsen effusion mass spectrometry

The behaviour of Cs and I during evaporation was analysed using a Knudsen effusion mass spectrometer, which was placed in an α-tight and lead-shielded glove box. The Knudsen cell consisted of a small tungsten crucible, positioned inside a high-temperature furnace and coupled to a QMG422 quadrupole mass spectrometer (Pfeiffer Vacuum GmbH, Germany),[49] which was equipped with a cross beam electron bombardment ion source. An electron energy of around 32 eV was selected for ionisation, striking a balance between avoiding excessive dissociation and achieving sufficient ionisation efficiency. The spectra were recorded in a temperature range from 530 to 2130°C, with a constant linear heating rate of approximately 7°C/min with a recording speed of 1 s/mass. Although the device can measure species up to 512 amu, this study focused primarily on $^{127}I^+$, $^{133}Cs^+$, $^{133}Cs^{127}I^+$, $^{238}U^+$, $^{238}U^{16}O^+$, $^{238}U^{16}O_2^+$ and $^{238}U^{16}O_3^+$ ionic species with additional recorded masses that are available in Supplementary

Information Note 1. Silver (Ag) was used as the reference material because its gaseous species are inert towards the analysed gas fractions. Due to instrument access issues not all uranium based species for the samples could be appropriately measured.

3. Results

3.1. Spark plasma sintering parameter and synthesis optimisation

SEM analysis of unsintered powders revealed that Nd doping directly affected the size of the nanoparticles produced from hydrothermal decomposition (see Supplementary Information Note 2). Specifically, increasing the amount of added Nd consistently resulted in a reduced the particle size. The charge compensation mechanism of Nd^{3+} incorporation into the UO_2 structure involves the oxidation of U^{4+} to the U^{5+} ion,[40,50] which has a smaller ionic radius.[41] Furthermore, in addition to the difference in grain size, variations in chemical composition also influenced the sintering process. In particular, an increase in the amount of Nd added resulted in a shift of the densification curves to higher temperatures. Subsequently the SPS parameters (temperature, time) had to be optimised to achieve a suitable microstructure, as well as the inclusion and more homogeneous distribution of CsI. Initial tests were conducted on all samples in argon atmosphere using the following parameters: heating at a rate of 100°C/min up to 1200°C, dwell of 1 minute and cooling at a rate of 200°C/min down to 400°C, followed by free cooling. However, electron microscopy of the subsequently examined samples revealed relatively large grains (>2 μm), so the intended microstructure was not present.

Subsequent optimised SPS conditions for the UO_2–(CsI) synthesis involved the following heating parameters: heating at a rate of 100°C/min to 800°C with a 1 min dwell, and then cooling to 400°C at a rate of 200°C/min followed by free cooling to room temperature. The $(U_{0.85}Nd_{0.15})O_2$–(CsI) sample was sintered with slightly modified parameters: heating at a rate of 100°C/min to 950°C with a 5 s dwell, and then cooling to 400°C at a rate of 200°C/min followed by free cooling to room temperature afterwards. In the sample, sintered at 950°C for 5 s, tiny CsI particles showed a much more homogeneous distribution throughout the

microstructure of the sample, consequently these SPS parameters were selected for sintering of all subsequent samples. The overview of the SPS parameters tested is presented in Table 1. Figure 1 shows the microstructures of the samples sintered at the selected (see Table 1) SPS parameters.

Table 1 – Tested SPS parameters during optimisation cycles. The parameters used for cycle No. 3 were selected for synthesising all subsequent samples in the present investigation.

<table>
<tr><th>Cycle №</th><th>Sintering piston pressure</th><th>Heating</th><th>Dwell</th><th>Cooling</th></tr>
<tr><td>1</td><td rowspan="3">71 MPa</td><td rowspan="3">100°C/min</td><td>1200°C; 1 min</td><td rowspan="3">200°C/min down to 400°C, followed by free cooling</td></tr>
<tr><td>2</td><td>800°C; 1 min</td></tr>
<tr><td>3 (selected)</td><td>950°C; 5 s</td></tr>
</table>

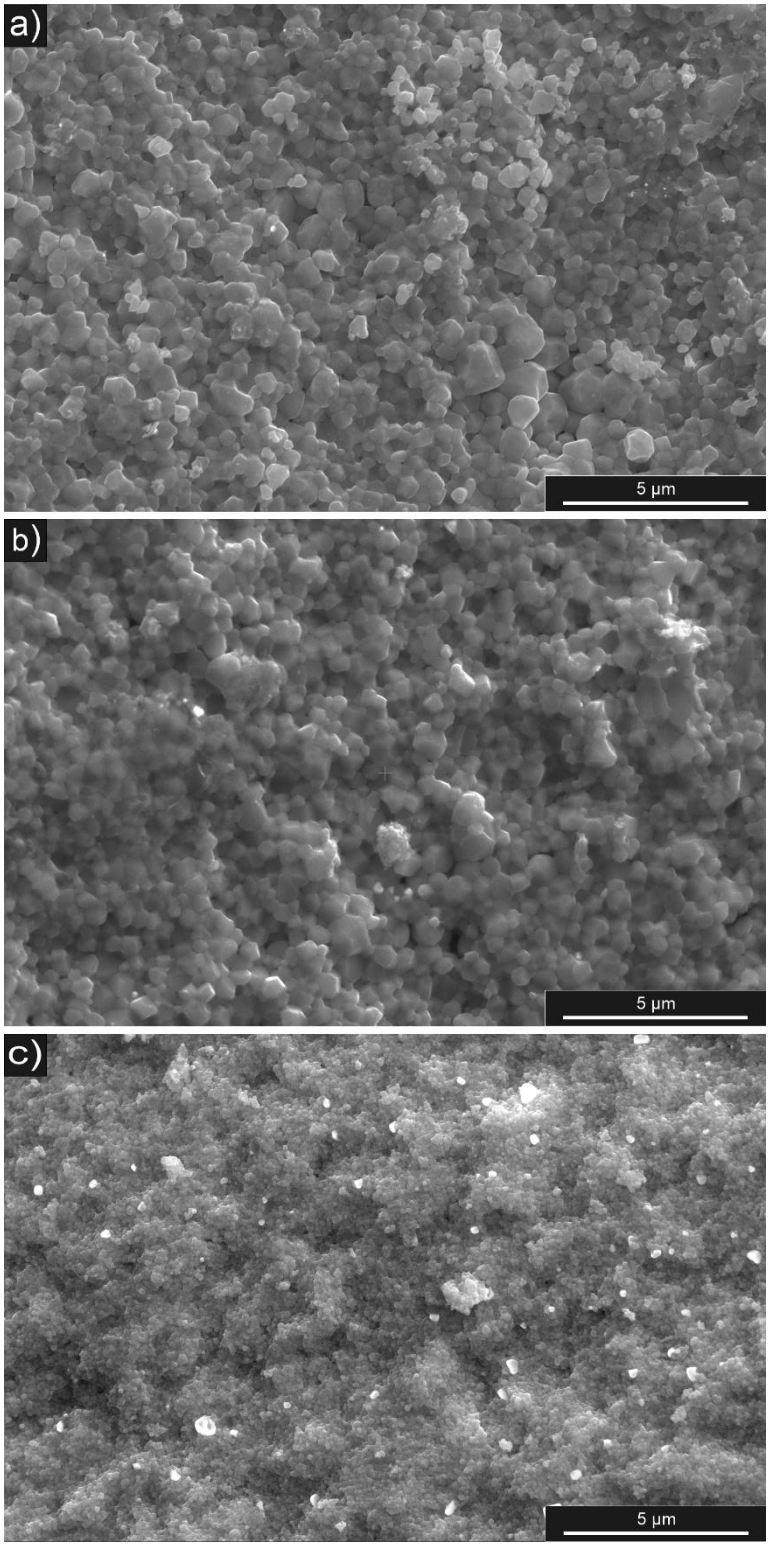


Figure 1 – SEM secondary electron (SE) images showing the microstructure of pellet cross-sections: a) UO_2–(CsI), b) $(U_{0.85}Nd_{0.15})O_2$–(CsI), and c) $(U_{0.7}Nd_{0.3})O_2$–(CsI), sintered using the SPS parameters selected in the Cycle 3 provided in Table 1. The bright white spots correspond to CsI particles.

Analysis of the sintered materials using ICP-MS showed that the concentrations of U and Nd corresponded to the targeted synthesis additions, within the limits of the ICP-MS measurement error. The Cs concentration was found to be between 0.9–2.1 mol %, although it should be noted that, despite the selected sintering parameters enabled a more homogeneous distribution of CsI particles to be achieved, their concentration within the sample still varied. It was not possible to directly measure I from ICP-MS, however in considering previous work[39] performed on the synthesis of pure UO_2 with CsI included via SPS, additions of I were found systematically corresponding Cs mol %. Nevertheless, the use of Nd may add inconsistencies, to this and as this is the first such study involving the Nd addition with Cs/I simultaneously, variations in the final Cs:I ratio may be possible. The Table 2 lists the compositions of the samples.

Table 2 – ICP-MS analysis results for quantitative determination of U, Nd and Cs present with investigated samples.

Sample	U, mol %	Nd, mol %	Cs, mol %
UO_2–(CsI)	100.00 ± 0.42	0.00 ± 0.42	0.936 ± 0.005
$(U_{0.85}Nd_{0.15})O_2$–(CsI)	85.62 ± 3.47	14.38 ± 3.47	1.400 ± 0.049
$(U_{0.7}Nd_{0.3})O_2$–(CsI)	65.36 ± 8.24	34.64 ± 8.24	2.069 ± 0.171

3.2. Material characterisation

X-ray powder diffraction

To determine the phase purity of the synthesised materials, XRD measurements at room temperature were performed and revealed that synthesised CsI-included Nd-doped UO_2 materials adopted single-phase structures consistent with fluorite UO_2. No secondary phases arising from, for instance, non-lattice incorporated Nd, CsI or Cs and I species could be resolved. The formation of a single-phase solid solution is consistent with previous studies considering the Nd doping levels.[40,51] The diffractograms as well as the Rietveld refinement profiles in the 2θ ranges of 20 – 70° are provided in Figure 2. Determined lattice parameters, as provided in Figure 2, indicate that the samples are partially oxidised beyond stoichiometric

values and would be best regarded as $(U_{1-y}Nd_y)O_{2+x}$–(CsI). This occurred because the sintering time of 5 s was too short to achieve a higher degree of stoichiometry in the O/M ratio.[52] To determine the oxygen excess in the samples, equation (1) from the literature,[53] which focuses on calculating the $(U_{1-y}Nd_y)O_{2+x}$ lattice parameter, was used.

$$a = \frac{4}{\sqrt{3}}\left\{(1-2y-2x)r_{U^{4+}} + (y+2x)r_{U^{5+}} + yr_{Nd^{3+}} + \frac{(2+x)}{2}r_{O^{2-}} - \frac{x}{2}r_{O^{V}}\right\} \times \left(1 - \frac{y}{200}\right), \quad (1)$$

with a – lattice parameter, y – Nd concentration from the ICP-MS measurements, x – oxygen excess, r – ionic radii.[41,54] Based on the calculations following x values in $(U_{1-y}Nd_y)O_{2+x}$ were determined: for the sample UO_2–(CsI) – 0.069(22); for the sample $(U_{0.85}Nd_{0.15})O_2$–(CsI) – 0.100(33) and for the sample $(U_{0.7}Nd_{0.3})O_2$–(CsI) – 0.047(22).

Thus, based on ICP-MS analysis and oxygen stoichiometry calculations, the final chemical formulas for the samples are as follows: $UO_{2.069}(CsI)_{0.009}$, $(U_{0.856}Nd_{0.144})O_{2.1}(CsI)_{0.014}$ and $(U_{0.654}Nd_{0.346})O_{2.047}(CsI)_{0.021}$, which for simplicity referred as Nd 0%, Nd 15% and Nd 30% respectively later in the text.

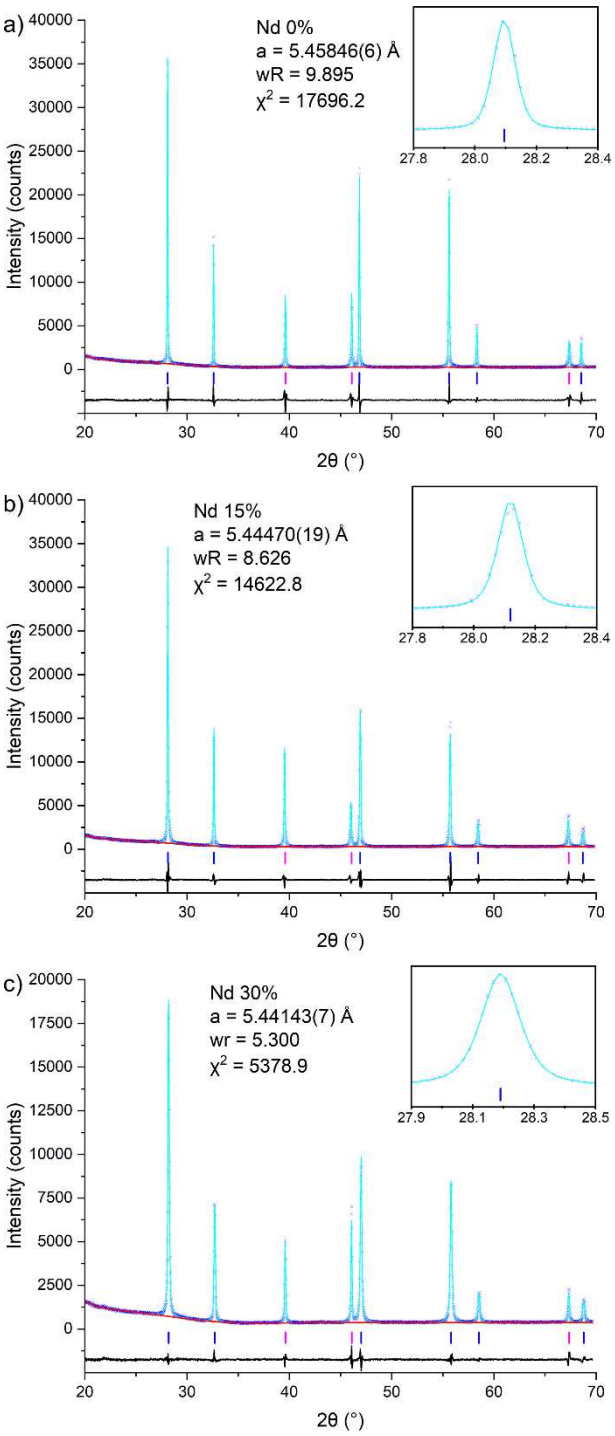


Figure 2 – Room temperature XRD diffractograms (blue) with Rietveld refinement profiles (cyan), background (red) and difference curves (black) for a) Nd 0%, b) Nd 15% and c) Nd 30% sintered for 5 s at 950°C in the 2θ range of 20 – 70°. Allowed reflections of the $Fm\bar{3}m$ space group for fluorite UO_2 and Pt are respectively represented by blue and purple markers. The graph insets show the main peak area crop.

Variable temperature X-ray diffraction

To verify the structural stability of the samples and confirm the consistency of their phase composition at high temperature, particularly as to whether they are stable and do not undergo temperature induced decomposition in vacuum or other phenomena that may impact subsequent KEMS investigations (described in subsequent sections), VT-XRD measurements were performed under vacuum conditions in range of 30 – 1150°C. The diffractograms for all measured compositions are provided in Figure 3.

Inspecting Figure 3, no additional or vanished peaks are observed in all diffractograms up to 1150°C under vacuum indicating that there is no loss of Nd or formation of secondary phases. The temperature dependence of the lattice parameters, as determined by Rietveld analysis illustrated in Figure 4, reveals a linear relationship as a function of temperature, which further indicates that there have been no changes to the structural chemistry of the investigated samples. For UO_2, changes in the linear expansion of the lattice parameter with temperature can indicate partial reduction or oxidation. For instance, under vacuum conditions, reduction and decomposition can be occur which would be indicated by a loss of the linear trend in lattice parameter thermal expansion. The observation of a linear trend in Figure 4 over the prescribed temperature range, indicates structural stability at higher temperatures and maintenance of the UO_2 structure without reduction or decomposition.

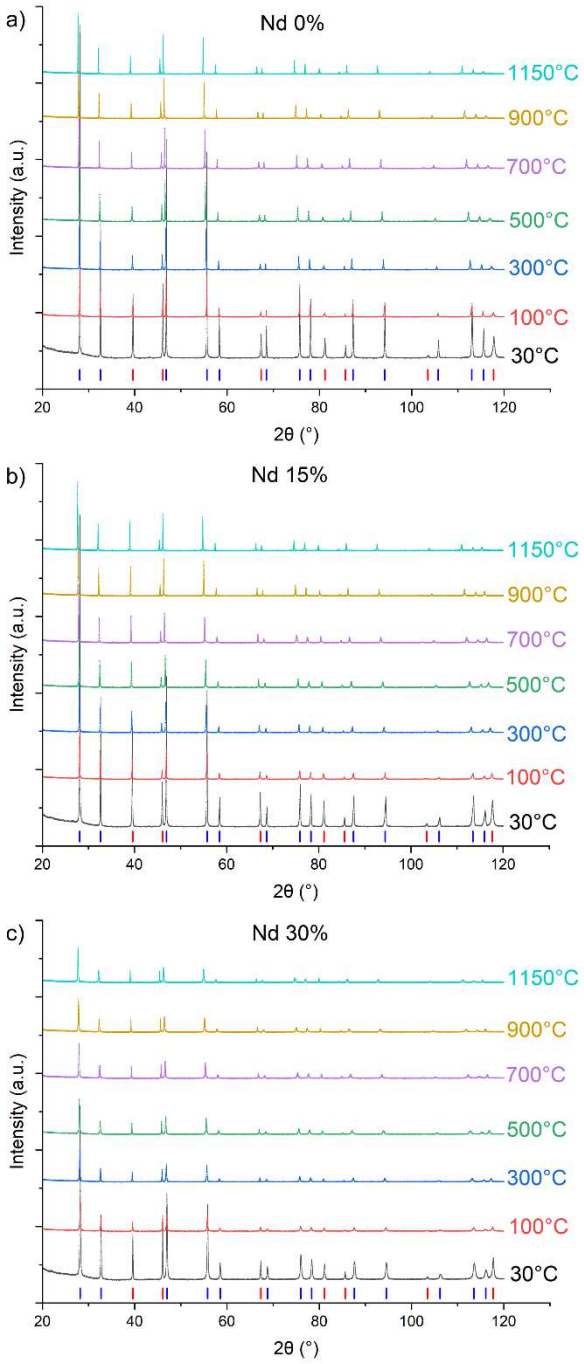


Figure 3 – VT-XRD diffractograms at different temperatures in vacuum for Nd 0%, Nd 15% and Nd 30%. Allowed reflections of the $Fm\bar{3}m$ space group for fluorite UO_2 and Pt are respectively represented by blue and red markers. With increasing temperature, a shift in the peaks towards lower 2θ values is observed.

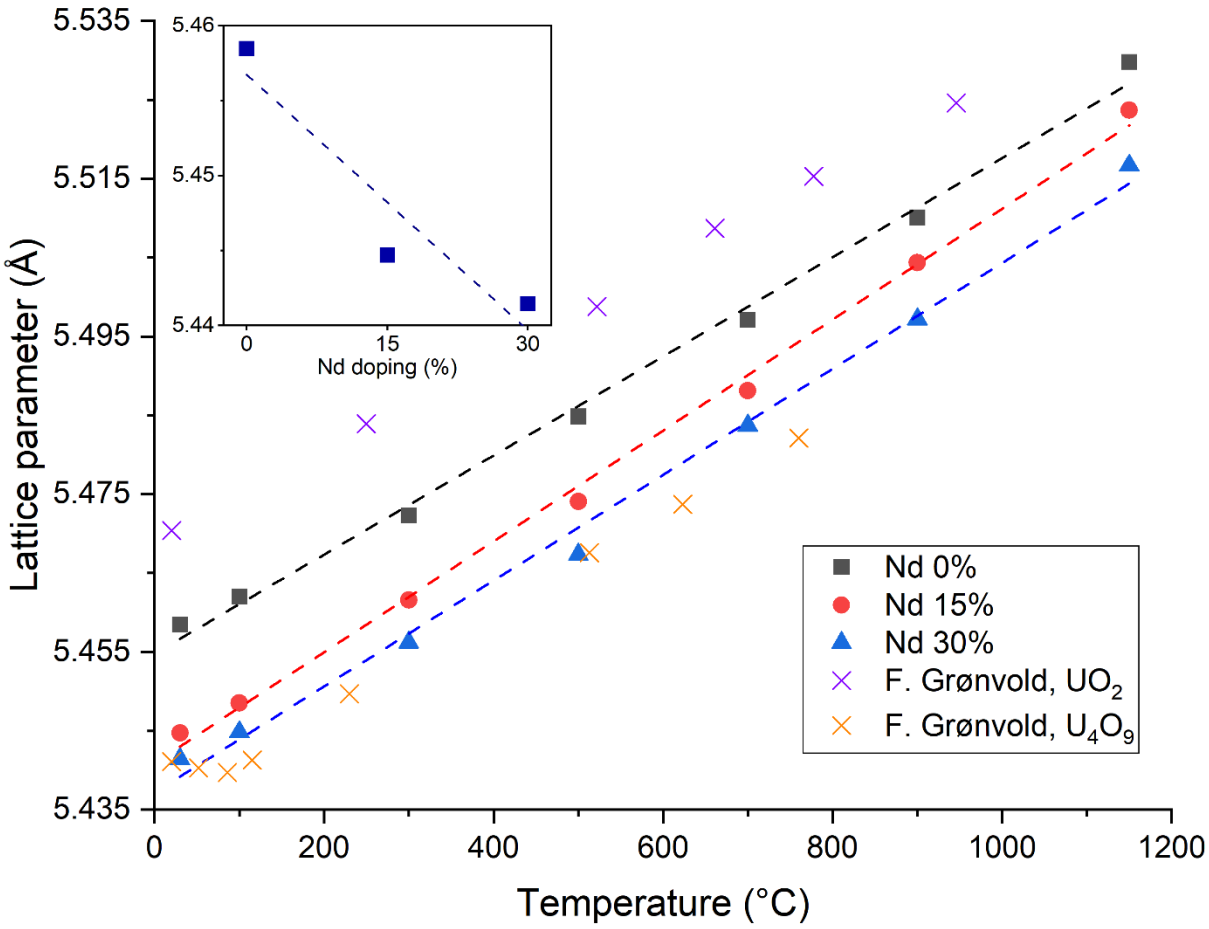


Figure 4 – Lattice parameter values as a function of temperature in range 30 – 1150°C determined by Rietveld analysis for the samples: Nd 0% (black), Nd 15% (red) and Nd 30% (blue), compared to the literature data.[55] The inset in the graph shows the dependence of the lattice parameter on the level of Nd doping in UO_2 at room temperature. Details of the linear fits shown by the dashed lines are provided in Supplementary Information Note 3.

3.3. Cs and I speciation in CsI-included Nd-doped UO_2

Electron microscopy and energy dispersive X-ray spectroscopy

To explore potential Nd-induced speciation of CsI away from its original state, EDX spectroscopy mapping was performed at different locations on the surface of the ceramic samples' cross-sections, two per sample. The regions were selected following a procedure whereby: 1 – at a location where a relatively large CsI particle (or several) was observed, and 2 – at a location where multiple fine CsI particles were observed. Maps were taken of the C K-edge, O K-edge, I L-edge, Cs L-edge, Nd L-edge, and U M-edge. Figures 5 – 7 show the

results of EDX mapping with maps of I and Cs unoverlaid for three samples: Nd 0%, Nd 15% and Nd 30% respectively with two different locations for each. The Supplementary Information Note 4 provides the overlaid maps, as well as an overview of the pellet cross-section indicating the mapping relative locations.

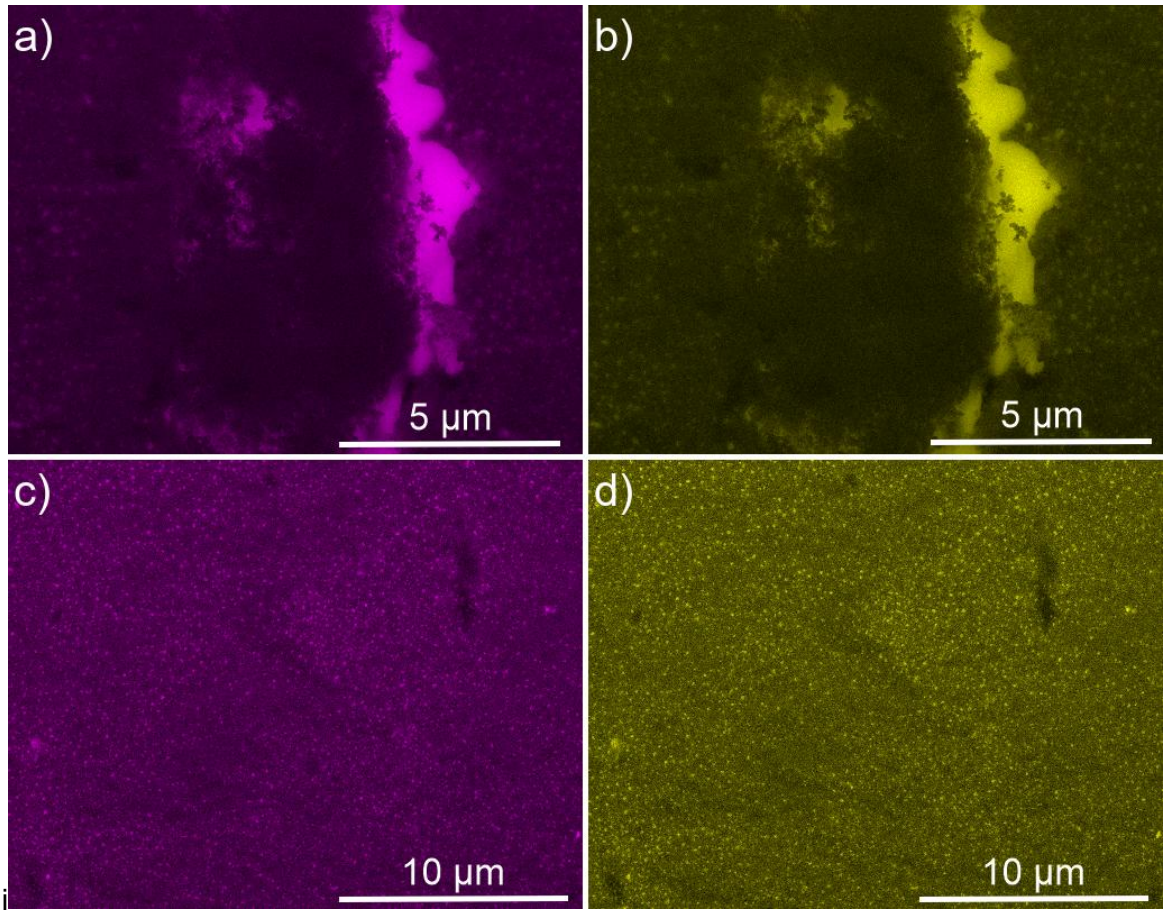


Figure 5 – EDX maps of I and Cs in two distinct locations for the Nd 0% sample. The maps show the EDX signal intensity of Cs (purple) and I (yellow) at two different locations on the surface of the pellet cross section (a, b, where a relatively large vein of CsI was found, and c, d, where CsI is more homogeneously distributed, respectively). Identical Cs and I distribution is apparent.

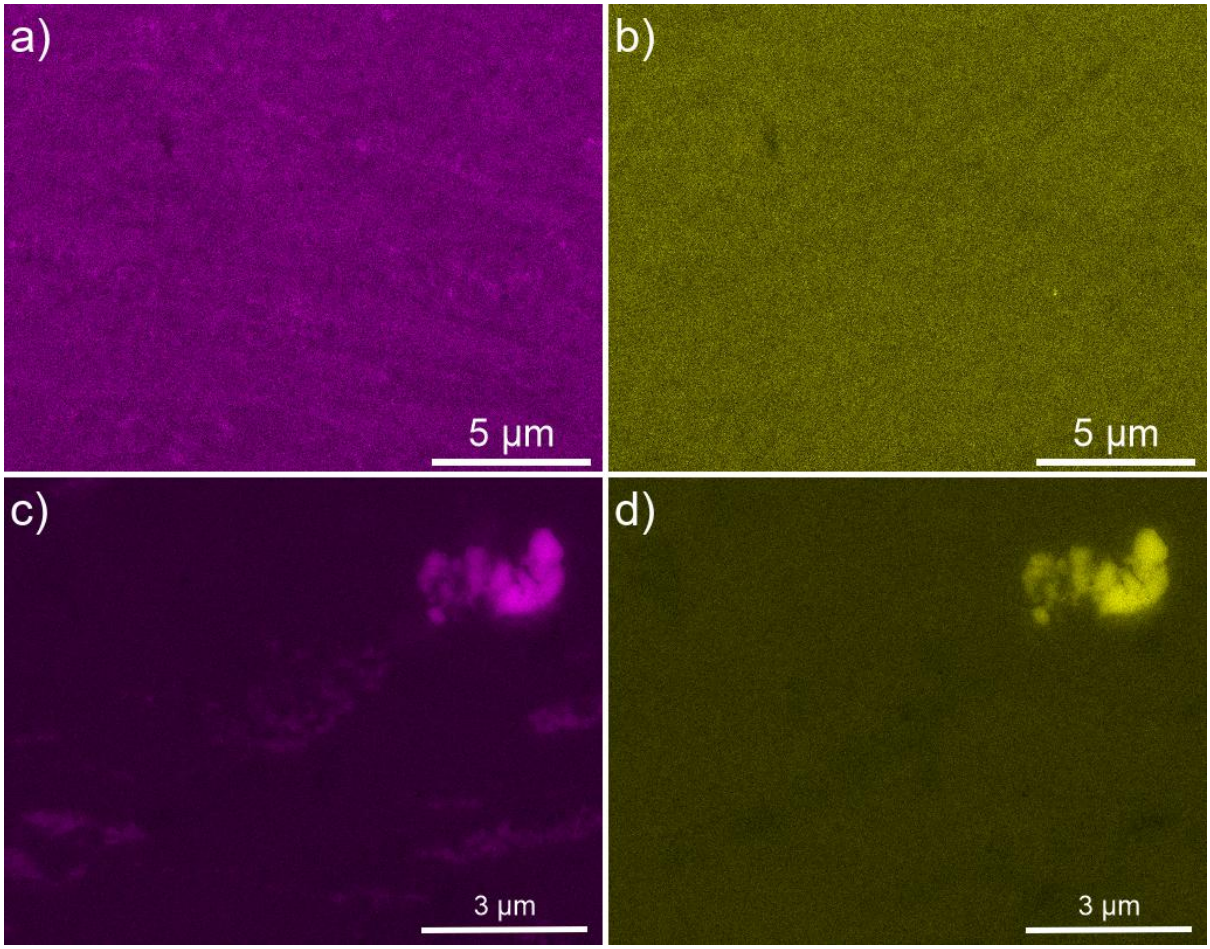


Figure 6 – EDX maps of I and Cs in two distinct locations for the Nd 15% sample. The maps show the EDX signal intensity of Cs (purple) and I (yellow) at two different locations on the surface of the pellet cross section (a, b, where CsI is more homogeneously distributed, and c, d, where a relatively large vein of CsI was found, respectively). In the presence of Nd, differences in the distribution of Cs and I are apparent. For instance, the bottom left, centre and bottom right quadrants and of c) compared to d) in addition to contrasting features in a) and b).

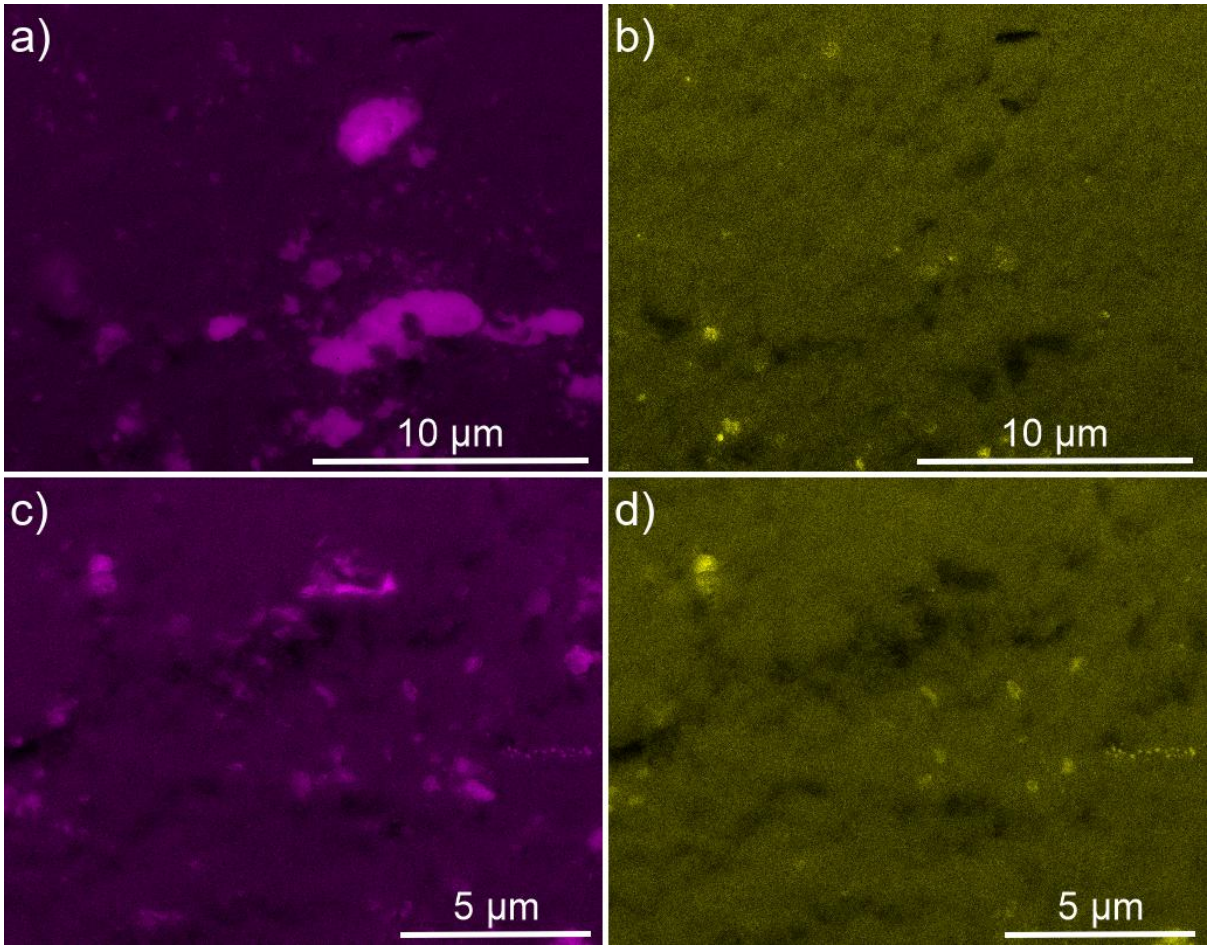


Figure 7 – EDX maps of I and Cs in two distinct locations for the Nd 30% sample. The maps show the EDX signal intensity of Cs (purple) and I (yellow) at two different locations on the surface of the pellet cross section (a, b, where a relatively large veins of CsI were found, and c, d, where CsI is more homogeneously distributed, respectively). Significant heterogeneous distribution of Cs and I can be readily observed between the maps indicating speciation of Cs and I away from the CsI initial state.

EDX mapping results showed that in the case of the Nd-free Nd 0% sample, the distribution of I and Cs always coincided, indicating that these elements remained in the form of CsI particles. Contrastingly, in the Nd 15% sample, mutually exclusive regions consisting of heightened amounts of Cs were observed. The fact that signals of Cs and I occur at different concentrations across the surface suggests that these elements have speciated beyond stoichiometric CsI states. In the higher Nd-doped Nd 30% sample, this speciation becomes more pronounced, as can be seen from the multiple more intense Cs areas. Moreover, the

use of numerous distinct examined regions in both Nd-doped and non-doped sample measurements, does strongly suggest variability in the speciation of CsI as Nd is introduced into the samples.

X-ray absorption spectroscopy. K-edge of Cs and I

To further probe the suspected speciation of CsI occurring with Nd doping of the investigated materials, XANES measurements were performed on the Cs and I K-edges. Using the K-edge for XANES analysis requires relatively higher X-ray energies (35.9846 keV and 33.1694 keV, respectively) as opposed to other edges. XANES measurements enable the bulk of the material to be appropriately probed, ensuring that associated measurement signals do not arise solely from the surface, as with EDX measurements. The Figure 8 provides the normalised K-edge XANES spectrograms for Cs and I in the Nd 0% and Nd 15% samples, plotted additionally using with a CsI standard.

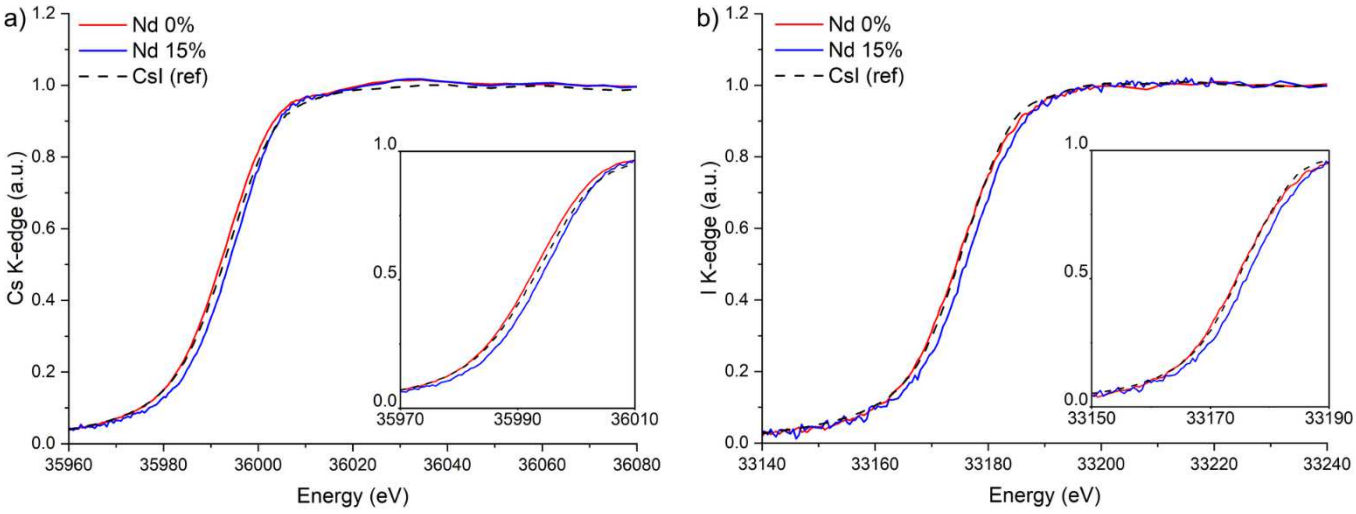


Figure 8 – Normalised XANES the K-edge spectra of a) Cs and b) I for the Nd 0% (red) and Nd 15% (blue) samples against the CsI (black dashed) standard. The slight shifts in the Nd-doped samples white line occurring for both Cs and I indicate a relatively different chemical environment for these elements compared to the CsI standard and between each sample.

When the K-edge XANES spectra of Cs and I are considered, subtle but significant variability is observed in the white line shape and shift of the Nd 15% sample compared to the undoped UO_2 sample and also the CsI standard. These results clearly indicate that, firstly, the added

CsI has readily dissociated from its original chemical compound state, and secondly, the chemistry of Cs and I differs between the Nd-doped and Nd-free samples, consistent with the SEM-EDX analysis. When the spectra of the two investigated samples are compared, it can be seen that the Nd-bearing sample shows a subtle shift of the white line towards higher energy at both the Cs and I K-edges. If the SEM-EDX measurements are followed, this indicates that partial oxidation of Cs and I is occurring in addition to their speciation. For instance, this could be explained by the presence of Cs-oxide or iodate (IO_3^-) phases, bearing in mind the more ionic nature of CsI. For instance, the presence partially oxidised Cs could be detected in case of the Cs-uranyl compounds formation,[56,57] while the partial occurrence of iodate species could potentially be stabilised by uranyl and or Nd species forming respectively uranyl and Nd-iodates, or by a combination of both.[58,59] In the case of the Nd-free Nd 0% sample, the white line on both the Cs and I K-edges more closely matches the CsI standard, consistent with the SEM-EDX analysis, indicating speciation has not occurred. Given the low sensitivity at the K-edge, this difference is not considered to be affecting the XANES results. Moreover, these measurements strongly support the SEM-EDX analysis indicating that Nd in the UO_2 structure contributes to the variable speciation of Cs and I.

3.4. Cs, I and CsI Release studies

Knudsen effusion mass spectrometry

In considering the combined SEM-EDX surface analysis with the Cs and I K edge XANES bulk measurements, the results of the investigation thus far show the addition of Nd into the UO_2 structure directly impacts the speciation of Cs and I. The observation that they exist in different chemical environments in the different Nd-doped samples suggests that their temperature-induced release should vary accordingly. Consequently, to investigate this hypothesis KEMS measurements were performed under the temperature range of 500 – 2130°C. Spectrograms of numerous gaseous species were obtained by vaporising samples in a Knudsen cell with using a mass spectrometer to measure the vapor signal. These species were selected for

measurement in advance and included I^+, Cs^+ and CsI^+, among others, which enabled determination of their behaviour during evaporation. Figure 9 shows the raw data on KEMS measured mass spectrometry signal as a function of temperature.

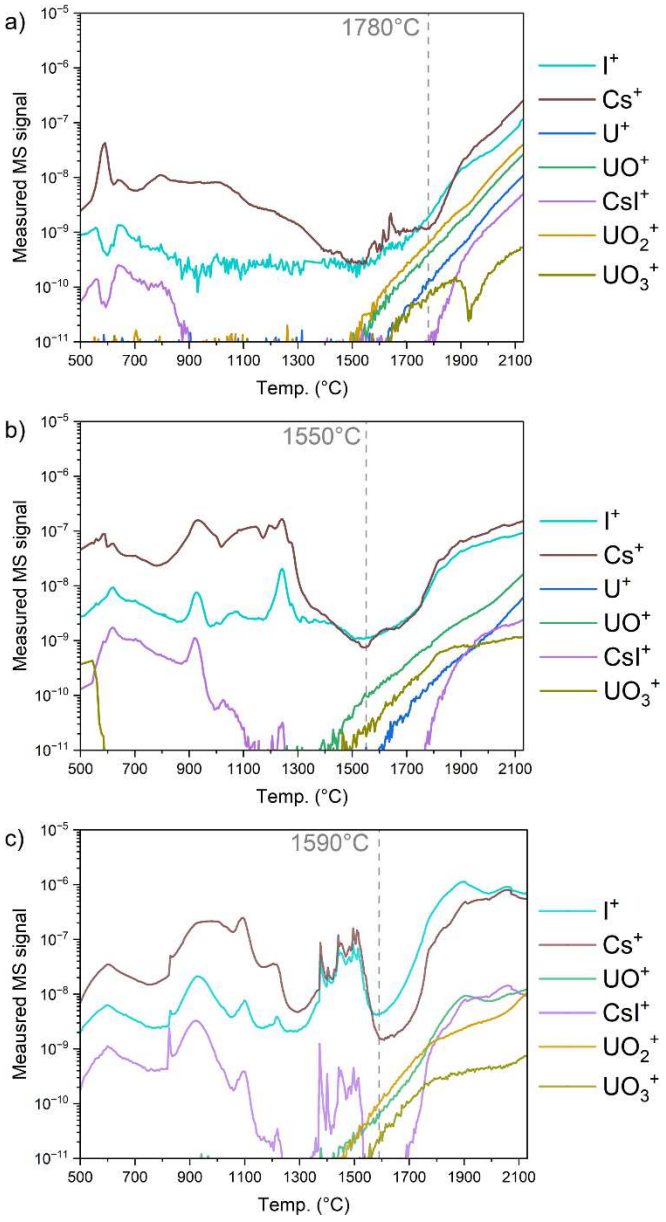


Figure 9 – Measured KEMS signal of various gaseous species as a function of temperature for a) Nd 0%, b) Nd 15% and c) Nd 30%. The grey vertical line indicates the approximate start of the final release of I^+ and Cs^+ caused by evaporation of the UO_2 matrix itself.

Based on the data in Figure 9, it is possible to assess qualitative characteristics of the Cs and I release. Three regions stand out from the main observations of the I^+, Cs^+ and CsI^+ curves

and from checking the CsI^+/I^+ and CsI^+/Cs^+ ratios (see Supplementary Information Note 5). The first region is up to 1200°C, where CsI melting occurs (632°C) and the evaporation of I^+, Cs^+ and CsI^+ gaseous species occurs mainly from the sample surface. The second region is the intermediate range between 1200°C and 1500°C, where CsI boiling occurs (1280°C) and evaporation mainly occurs due to cracking of the sample. The third region is the final release region from 1500°C, when the sample matrix itself starts to evaporate. The high release in the latter region is explained by the high density of the sintered samples, which hinders gas diffusion at lower temperatures. Consequently, reaching evaporation of the UO_2 matrix exposes the intergranular CsI inclusions, initiating their release.

An important observation here is the difference in the onset temperatures of this final release. The differences between samples Nd 0% and Nd 15% could be explained by different oxygen hyperstoichiometry (see section 3.2), which is known to promote an earlier release.[60] However, the differences between samples Nd 0% and Nd 30%, the latter of which has lower oxygen hyperstoichiometry, can be explained by the presence and quantity of Nd. Therefore, in addition to its previously described influence on CsI speciation and microstructure, Nd evidently favours a shift in release towards lower temperatures.

The effect of Nd can also be seen in the patterns observed during the final release, including both Cs^+, I^+ and the signals related to the UO_2 matrix. In Nd-free Nd 0% sample in particular, the signals continue to rise sharply even when the maximum measured temperature is reached. However, in the case of the Nd-doped samples, saturation is already observed in Nd 15% sample at this temperature, while in Nd 30% sample the signals reach a plateau. Although not all UO_2-related cation signals were collected for some samples, those that were measured is sufficient to identify differences in final release. The next important observation relates to the CsI^+/I^+ and CsI^+/Cs^+ ratios (see Supplementary Information Note 5). By the time of the final release, the I^+ and Cs^+ converge. However, it was also observed that during final release the CsI^+/I^+ and CsI^+/Cs^+ signal ratios decreased with increasing Nd content. Furthermore, in Nd

30% sample, the I^+ signal becomes higher than the Cs^+ signal. This behaviour suggests that chemical changes occur in the presence of Nd at high temperatures that affect the release of Cs and I. Moreover, although CsI is still present in the samples, the CsI^+/I^+ and CsI^+/Cs^+ signal ratios indicate that in the samples containing Nd, the release of Cs and I does not originate solely from CsI.

Fractional release analysis

Based on the obtained spectrograms, Normalised Instantaneous Release (NIR) and Normalised Fractional Release (NFR) were also calculated in accordance with equations (2) and (3) respectively,[28] which should be noted as being simplified for relative qualitative comparison.

$$NIR(t_i) = \frac{I\sqrt{T}}{\max(I\sqrt{T}\forall T)} \tag{2}$$

$$NFR(t_i) = \frac{\int_0^{t_i} I\sqrt{T}dt}{\int_0^{t_{end}} I\sqrt{T}dt} \tag{3}$$

with I – measured mass spectrometry signal, T – temperature, and t_i – time of the recording.

The NIR is defined as the differential effusion flow, measured in terms of the amount of vapour species present per unit time at a given temperature, and is subsequently normalised to the highest peak of the given release. The NFR is defined as the integral of the instantaneous release, at a given temperature, which is normalised to the value at the end of the release.

NIR and NFR calculations enable the transition from raw KEMS data to quantitative evaluations of gaseous fraction release from the sample. Figure 10 provides the results of the KEMS data analysis with calculated NIR and NFR of I^+, Cs^+ and CsI^+ gaseous species for all three samples.

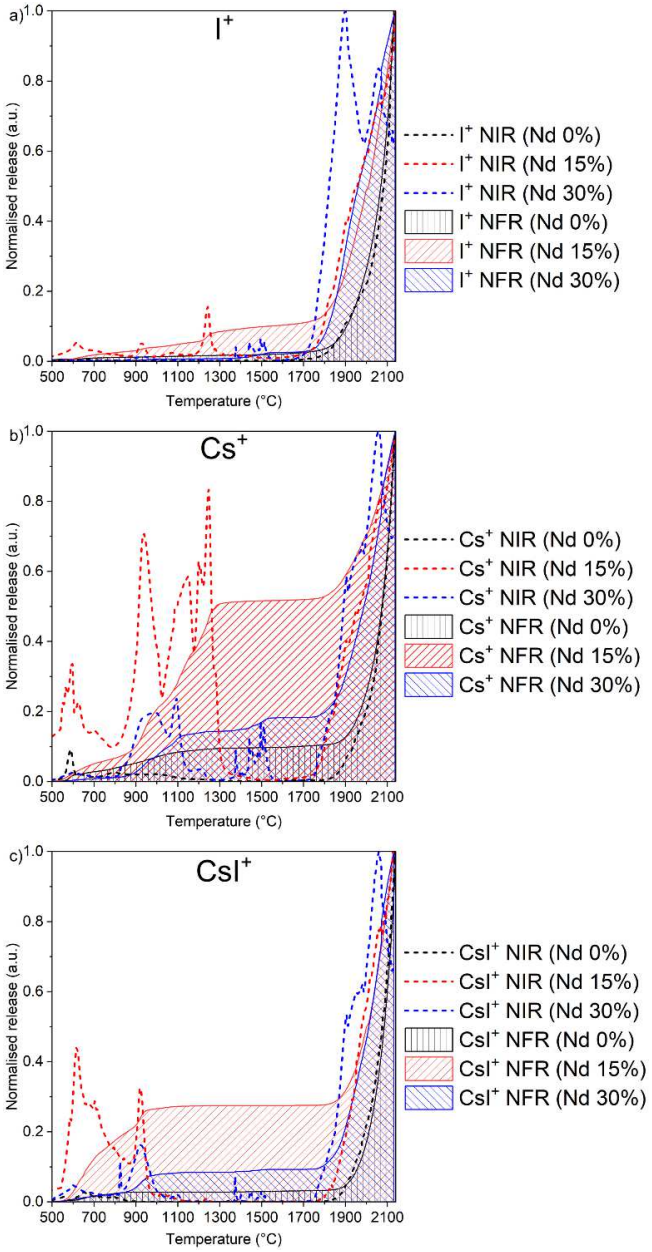


Figure 10 – NIR and NFR of a) I^+, b) Cs^+ and c) CsI^+ gaseous species for Nd 0%, Nd 15% and Nd 30% reffered as: Nd 0% (black), Nd 15% (red) and Nd 30% (blue) respectively.

The NIR data confirm the previously observed behaviour of I^+, Cs^+ and CsI^+ at UO_2 matrix evaporation temperatures, where the temperatures at which the final evaporation of these gaseous species begins are lower, the more Nd is present. Here, it is also pertinent to consider the spikes in the NIR curves at lower temperatures in Figure 10. As described in the previous section, the peaks observed below the final release temperature of 1500°C are attributed to the presence of pure CsI (or other Cs-, I-based compounds) at the surface of the sample as

well as to the propagation of cracks in the heated sample, accompanied by a sharp release of exposed material, which can be also seen from the total amount of material in the NFR graph. The significant differences in patterns and quantitative values between the samples further confirm the influence of Nd on the behaviour of Cs and I during release. Furthermore, the similar patterns of I^+, Cs^+, and CsI^+ in the Nd-free sample suggest that these gas fractions mostly originate from CsI particles. Conversely, in the Nd-doped Nd 15% and Nd 30% samples, the normalised release curves of I^+, Cs^+, and CsI^+ differ significantly, especially in the high-temperature region. Such behaviour in Nd-doped samples may indicate the formation of secondary phases caused by reactivity between Cs/I and U/Nd. However, the upper measurement limit of the instrument is 512 amu which limits the ability to measure potential gaseous species such as dicaesium uranate ($Cs_2UO_4^+$, 576 amu) or Nd-iodide (NdI_3^+, 523 – 527 amu, depending on the Nd isotope), while no other compounds with molecular weights <512 amu were detected. Nevertheless, the results of the KEMS data analysis generally support the observations made by SEM and XANES analysis: the presence of Nd in UO_2 influences the chemistry of Cs and I and further appears to have an impact their thermal release during evaporation depending on the Nd content.

4. Discussion

This investigation has demonstrated that the incorporation of CsI into SPS synthesised $(U_{1-y}Nd_y)O_2$–(CsI) for y = 0, 15 and 30% nanoceramics is a chemically variant process, whereby increasing amounts of Nd appear to result in increased speciation of CsI. This effect can be influenced by a number of synthesis parameters, however optimised control of SPS sintering steps and subsequent post-analysis revealed comparable specimen characteristics such that associated chemical observations can be primarily attributed to the effect of Nd. Pertinently, via KEMS measurements on these materials it was found that the behaviour of temperature-induced CsI release correlates with the presence of Nd. Specifically, increasing Nd concentrations or more enhanced CsI speciation, results in a lower temperature for which

Cs, I and CsI are released compared to the Nd-free case. Nevertheless, it is necessary to discuss and consider the potential chemical origins of how this solid solution behaviour can impact release. For higher Nd doping the speciation of CsI indicates they form chemically distinct phases whereby the potential formation of secondary phases containing Cs and I may arise due to their reactivity with elements of the UO_2 matrix (Nd and U) and subsequent precipitation. Incorporation of Cs and I within the UO_2 matrix is largely ruled out as a leading effect, due to their known low solubility. Some studies have proposed the possible reactivity of Cs with U forming Cs_2UO_x from thermodynamic calculations and experimental observations.[56,57,61] The free I produced in this way could either evaporate as $I_2\uparrow$ or react with Nd to form intermetallic NdI_3 or another mixed U/Nd-based intermetallic or oxide compounds. Subsequently, chemical reactivity with Nd can also be expected particularly since, despite the formation of a solid solution between Nd and UO_2, studies show that Nd tends to migrate towards grain boundaries,[62,63] where it can react with Cs/I. Crucially, nano-sized grains, as found in HBS, amplify this effect by reducing the migration distance to the boundary. Thus, enhancing surface reactivity between Nd and Cs/I. Furthermore, the presence of a trivalent lanthanides in UO_2 is known to result in a general increase of the oxygen potential in the context of fuel.[64] With regard to general model materials, during long in-furnace sintering, the oxygen potential of the sample and the sintering atmosphere equilibrate;[65] however, in the case of relatively rapid SPS, such equilibrium might not be reached and the oxygen potential of the samples is dictated by the chemistry of the dopant rather than the sintering atmosphere, concordant to the behaviour in fuel. Consequently, as the Nd-doping level increased, the oxygen potential of the samples is raised. This may consequently be an indirect contributing factor of the Nd occurrence leading to the oxidation based CsI speciation of CsI with the further potential reactivity between U/Nd and Cs/I.[61] In addition to the potential formation of phases via such reactivity, there is also the possibility of Nd influencing CsI through van der Waals forces. These effects arise because Cs and I are both heavy, highly polarisable ions[66] and van der Waals dispersion between such species is non-negligible compared to the total cohesive

energy in soft ionic lattices and related materials. Critically these forces directly impact detachment and release at specific temperatures. Changes to the chemical structure of the UO_2 lattice, such as via the aliovalent substitution of U^{4+} for Nd^{3+} generating U^{5+} can readily result in a change to the van der Waals interactions, and this effect is also amplified by the migration of Nd to the boundaries of the nanograins. It is conceivable that such concentrations of Nd along the surface of the UO_2 nanograins which contact CsI can impact the subsequent van der Waals interactions leading to modulation of the CsI bonding and subsequent speciation. Particularly, Nd^{3+} would be expected to lower the local charge density when found more concentrated on the surface of the nanograins than U^{4+}, leading to reduced interactions and retention with I^{-1}. It is noteworthy that the amount of Nd influences the microstructure, particularly grain size of the precursor powder material prior to SPS (see Supplementary Information Note 2). Specifically, as the content of Nd increases, there is a reduction in grain size of the examined materials, this can in turn affect the oxygen uptake and stoichiometry of materials. However, oxygen stoichiometry calculations showed similar values, with relatively marginal discrepancy, and consistent VT-XRD behaviour. Nevertheless, the use of high doping amounts of Nd is a more prominent and considered major variable between the examined samples. Accordingly, the speciation of CsI can result from of a variety of factors, critically however, these are driven by the chemistry and inclusion of Nd in the materials.

Studies that employed KEMS analysis to investigate the temperature-induced release of CsI from UO_2 model materials sintered using SPS showed a single early release of Cs and I (in the range of 530 to 1130°C).[22,29] However, these studies did not focus on nanoceramics, where the average grain sizes were an order of magnitude larger than that of the materials investigated here.[39] Smaller grain sizes should result in faster CsI release due to a much higher grain boundary density. Furthermore, these studies did not examine the effect of Nd or related UO_2 lattice matrix-soluble elements via model materials. In those investigations, lower-temperature release of the matrix was generally observed for the SPS-synthesised UO_2 materials compared to the present study. Notably, this appears to be the first study to have

examined the effect of UO_2 nanoceramics on CsI, in addition to Nd incorporated as a solid solution. Compared to the aforementioned model system studies, final CsI release occurs at comparatively higher temperatures (without considering Nd). This could be attributed to the effect of nanograins, but is likely more related to better compacted material, which retains CsI within the structure slowing its release up to high temperatures. When considering the effect of Nd in the present investigation and taking into account that the synthesised compounds have similar densities, differences are observed between when Nd is present or absent. Particularly, the samples Nd 15% and Nd 30% possess obviously non-coincident I^+, Cs^+, and CsI^+ release behaviour that is not found in the release spectrum of the Nd-free Nd 0% sample. This could indicate the release occurring from Cs- and I-based compounds formed as a result of the reactivity between these elements with Nd or U. Another important observation is that the final release of all the gaseous species measured shifts towards lower temperatures as the Nd content increases. Studies on the vaporisation of irradiated nuclear fuel with high burn-up (55 – 67 GWd/tHM) show that the release profiles of I and Cs exhibit greater release at higher temperatures (>1230°C),[22] which is pertinently closer to the Nd-doped compositions of the present investigation. Previous work on very high burn-up SNF (240 GWd/tHM) demonstrated that the release patterns of Cs and I measured by KEMS exhibited a more similar behaviour and two peaks: in the region of ~730°C and of ~1230°C, similar to the findings in the present study.[32] However, the temperature-induced release of IRF-related elements is influenced by a multitude of factors inherent in the complexity of SNF, for instance, arising from the fuel's irradiation history, as well as its chemical, microstructural, thermal, and physical characteristics. Decoupling these effects and cross-comparing SNF specimens towards determining underlying chemical-physical mechanisms is extremely difficult from a direct investigative perspective. Contrastingly, the current investigation builds upon previous studies of CsI-included UO_2 model material work by doping with Nd as a proxy for the examining the behaviour of matrix-soluble minor actinides and FPs, simultaneously with the influence of a nanostructure similar to HBS. The results show more agreement with that of

higher burn-up irradiated fuel studies. Considering that CsI speciation is also expected from γ-radiation,[22,23] it would appear, that not just radiological, but also chemical processes within irradiated fuel, particularly in HBS regions have an impact on the chemistry and subsequent release of Cs, I, and potentially other IRF-related elements. This naturally has pertinent implications for the use and storage of nuclear fuel, particularly of which are intended for high burn up cycles, that is currently being pursued by many nations.

5. Conclusions

This investigation has examined the chemistry of CsI within SPS-synthesised CsI-bearing UO_2 nanoceramics through Nd doping variation towards replicating the conditions of the HBS in irradiated nuclear fuel with high burn-up. The results demonstrated the gradual and continual speciation of CsI as a result of Nd incorporation within the bulk material and subsequently affects the temperature-induced release of I^+, Cs^+ and CsI^+. As shown by a combination of XANES spectroscopy on the Cs K-, and I K-edges and SEM-EDX analysis, CsI in presence of Nd is found to speciate into individual phases. Considering the chemistry of the materials it is suspected Cs and I adopt phases that are either separate, oxidised or involve the reactivity with the Nd-doped UO_2 lattice matrix. KEMS measurements and analysis provided release spectrums from examined compositions, where the temperature of final release of I^+, Cs^+, and CsI^+ gaseous species is shifted towards lower temperatures with increasing Nd content. Additionally, the release profiles indicate they possess features which are consistent non-CsI species, such as secondary phases arising from initial speciation and reactivity. When the results are compared with those of previous studies on the CsI release in model systems[22,29] and irradiated fuel,[22,32] more agreement is found with the latter. It has been previously established that γ-radiation induces speciation of CsI within SNF which subsequently affects its release.[22] The present study demonstrates that the CsI stability and speciation are affected not only radiologically affected, but also chemically within the UO_2 matrix resembling that of the HBS. This work provides critical fundamental understanding into the behaviour of CsI

within high burn-up irradiated fuel and how changes to the local chemistry and microstructure of the fuel, via the formation of the HBS and subsequent enhanced FPs inventory, can affect the release mechanisms of IRF-related elements including Cs and I, which constitutes a crucial aspect of SNF management safety.

6. Author contributions

The project was conceived and developed by Daniil Shirokiy and Gabriel L. Murphy. Research methodology, experimental planning and formal analysis were conducted by Daniil Shirokiy, Karin Popa and Gabriel L. Murphy. Supervision and funding acquisition was performed by Dirk Bosbach, Karin Popa and Gabriel Murphy. Synthesis of materials was done by Karin Popa, Daniil Shirokiy and Marco Cologna. X-ray diffraction was performed by Olaf Walter and Karin Popa. Electron microscopy imaging was performed by Felix Brandt, Martina Klinkenberg, Walter Bonani, Ana Isabel Martinez Ferri and Daniil Shirokiy. X-ray absorption spectroscopy was performed by Damien Prieur. Knudsen effusion mass spectrometry was performed by Jean-Yves Colle, Ondřej Beneš, and Daniil Shirokiy. Inductively coupled plasma mass spectrometry was performed by the in-house Analytical Service at the JRC Karlsruhe led by Răzvan Buda. Manuscript writing, and editing was performed by Daniil Shirokiy and Gabriel L. Murphy with input by all co-authors.

7. Acknowledgements

The experimental data used in this research were partly generated through access to the ActUsLab FMR under the Framework for access to the Joint Research Centre physical Research Infrastructures of the European Commission (Cassius project, Research Infrastructure Access Agreement N° 36618/03). The authors are grateful to the funding and support from the Helmholtz Graduate School for Energy and Climate Research (HITEC) at Forschungszentrum Juelich GmbH. The authors acknowledge Herwin Hein and Thomas Gouder for carrying out the supporting measurements, and Victor Vinograd for the productive discussions regarding the CsI speciation. The authors are grateful to funding and support from

the German Federal Ministry of Federal Ministry for Research, Technology and Aeronautics (BMTFR) under funding code 02NUK088A for Project Transient which has supported this research. The authors are also grateful for the funding and support from EURAD 2 working package SAREC grant number ID: 101166718.

8. Data availability

Data is available on request.

9. References

1 Karoutas, Z. *et al.* The maturing of nuclear fuel: Past to Accident Tolerant Fuel. *Prog Nucl Energ* **102**, 68-78 (2018). https://doi.org/10.1016/j.pnucene.2017.07.016

2 Kashibe, S. & Une, K. Effect of additives (Cr_2O_3, Al_2O_3, SiO_2, MgO) on diffusional release of ^{133}Xe from UO_2 fuels. *J Nucl Mater* **254**, 234-242 (1998). https://doi.org/10.1016/S0022-3115(97)00356-5

3 Wright, J., Arborelius, J. & Backman, K. Development of Westinghouse advanced doped pellet technology. Report No. HPR-364-V2, 203-217 (Lillehammer, Norway, 2005).

4 Cole, S. E., Delafoy, C., Graebert, R., Louf, P. H. & Teboul, N. AREVA optimized fuel rods for LWRs. *TopFuel, Manchester, UK* (2012).

5 Lassmann, K., Walker, C. T., Vandelaar, J. & Lindstrom, F. Modeling the High Burnup UO_2 Structure in LWR Fuel. *J Nucl Mater* **226**, 1-8 (1995). https://doi.org/10.1016/0022-3115(95)00116-6

6 Sonoda, T. *et al.* Transmission electron microscopy observation on irradiation-induced microstructural evolution in high burn-up UO_2 disk fuel. *Nucl Instrum Meth B* **191**, 622-628 (2002). https://doi.org/10.1016/S0168-583x(02)00622-5

7 Rondinella, V. V. & Wiss, T. The high burn-up structure in nuclear fuel. *Mater Today* **13**, 24-32 (2010). https://doi.org/10.1016/S1369-7021(10)70221-2

8 Mogensen, M., Pearce, J. H. & Walker, C. T. Behaviour of fission gas in the rim region of high burn-up UO_2 fuel pellets with particular reference to results from an XRF investigation. *J Nucl Mater* **264**, 99-112 (1999). https://doi.org/10.1016/S0022-3115(98)00474-7

9 Barner, J., Cunningham, M., Freshley, M. & Lanning, D. HBEP-61. *Battelle Pacific Northwest Laboratories* (1990).

10 Noirot, J. *et al.* High burnup changes in UO_2 fuels irradiated up to 83 GWd/t in M5® claddings. *Nucl Eng Technol* **41** (2009). https://doi.org/10.5516/NET.2009.41.2.155

11 Fast / Instant Release of Safety Relevant Radionuclides from Spent Nuclear Fuel FIRST-Nuclides. Final scientific report. Report No. 5.13, (Collarborative project, Karlsruhe, Germany, 2015).

12 Johnson, L., Ferry, C., Poinssot, C. & Lovera, P. Spent fuel radionuclide source-term model for assessing spent fuel performance in geological disposal. Part I: Assessment of the instant release fraction. *J Nucl Mater* **346**, 56-65 (2005). https://doi.org/10.1016/j.jnucmat.2005.04.071

13 Konings, R. J. M., Wiss, T. & Beneš, O. Predicting material release during a nuclear reactor accident. *Nat Mater* **14**, 247-252 (2015). https://doi.org/10.1038/nmat4224

14 Spent Fuel Evolution under Disposal Conditions: Sythesis of Results from the EU Spent Fuel Stability (SFS) Project. Report No. NTB 04-09, (National Cooperative for the Disposal of Radioactive Waste (NAGRA), Wettingen, Switzerland, 2005).

15 Nordström, E. Fission gas release data for Ringhals PWRs. Report No. TR-09-26, (Swedish Nuclear Fuel and Waste Management Co (SKB), Stockholm, Sweden, 2009).

16 Johnson, L., Garisto, N. & Stroes-Gascoyne, S. Used fuel dissolution studies in Canada. *Waste Management* **85**, 479-481 (1985).

17 Kleykamp, H. The Chemical-State of the Fission-Products in Oxide Fuels. *J Nucl Mater* **131**, 221-246 (1985). https://doi.org/10.1016/0022-3115(85)90460-X

18 Ferry, C. *et al.* Synthesis on the spent fuel long term evolution. Report No. CEA-R-6084, (Commissariat à l´Énergie Atomique, Saclay, France, 2005).

19 Finn, P. A., Hoh, J. C., Wolf, S. F., Slater, S. A. & Bates, J. K. The release of uranium, plutonium, cesium, strontium, technetium and iodine from spent fuel under unsaturated conditions. *Radiochim Acta* **74**, 65-71 (1996). https://doi.org/10.1524/ract.1996.74.special-issue.65

20 Besmann, T. M. & Lindemer, T. B. Chemical Thermodynamics of the System Cs-U-Zr-H-I-O in the Light Water Reactor Fuel-Cladding Gap. *Nucl Technol* **40**, 297-305 (1978). https://doi.org/10.13182/NT78-A26727

21 Spahiu, K. State of the Knowledge (SoK) Report Spent Nuclear Fuel Report No. Domain 3.1.1, (EURAD, Gothenburg, Sweden, 2021).

22 Colle, J. Y. *et al.* Cesium and iodine speciation in irradiated UO_2 fuel. *J Nucl Mater* **608**, 155715 (2025). https://doi.org/10.1016/j.jnucmat.2025.155715

23 Cubicciotti, D. & Davies, J. H. The release of iodine from iodide salts by gamma radiolysis. *Nuclear Science and Engineering* **60**, 314-319 (1976).

24 Serrano-Purroy, D. *et al.* Instant release fraction and matrix release of high burn-up UO_2 spent nuclear fuel: Effect of high burn-up structure and leaching solution composition. *J Nucl Mater* **427**, 249-258 (2012). https://doi.org/10.1016/j.jnucmat.2012.04.036

25 Schreinemachers, C. *et al.* Caesium and iodine release from spent mixed oxide fuels under repository relevant conditions: Initial leaching results. *Mrs Adv* **7**, 100-104 (2022). https://doi.org/10.1557/s43580-022-00220-7

26 Johnson, L. *et al.* Rapid aqueous release of fission products from high burn-up LWR fuel: Experimental results and correlations with fission gas release. *J Nucl Mater* **420**, 54-62 (2012). https://doi.org/10.1016/j.jnucmat.2011.09.007

27 Park, G. I. *et al.* Hot Experiment on Fission Gas Release Behavior from Voloxidation Process using Spent fuel. Report No. KAERI/TR-3448/2007, (Korea Atomic Energy Research Institute, Daejeon, Republic of Korea, 2007).

28 Colle, J. Y. *et al.* Comparative study of fission product release of homogeneous and heterogeneous high-burn up MOX fuel by Knudsen Effusion Mass Spectrometry supported by EPMA, SEM/TEM and thermal diffusivity investigations. *J Nucl Mater* **578**, 154340 (2023). https://doi.org/10.1016/j.jnucmat.2023.154340

29 Di Lemma, F. G., Colle, J. Y., Rasmussen, G. & Konings, R. J. M. Fission product partitioning in aerosol release from simulated spent nuclear fuel. *J Nucl Mater* **465**, 127-134 (2015). https://doi.org/10.1016/j.jnucmat.2015.06.002

30 Colle, J. Y., Hiernaut, J. P., Papaioannou, D., Ronchi, C. & Sasahara, A. Fission product release in high-burn-up UO_2 oxidized to U_3O_8. *J Nucl Mater* **348**, 229-242 (2006). https://doi.org/10.1016/j.jnucmat.2005.09.024

31 Hiernaut, J. P., Wiss, T., Papaioannou, D., Konings, R. J. M. & Rondinella, V. V. Volatile fission product behaviour during thermal annealing of irradiated UO_2 fuel oxidised up to U_3O_8. *J Nucl Mater* **372**, 215-225 (2008). https://doi.org/10.1016/j.jnucmat.2007.03.174

32 Hiernaut, J. P. *et al.* Fission product release and microstructure changes during laboratory annealing of a very high burn-up fuel specimen. *J Nucl Mater* **377**, 313-324 (2008). https://doi.org/10.1016/j.jnucmat.2008.03.006

33 Kegler, P. *et al.* Chromium Doped UO_2-Based Ceramics: Synthesis and Characterization of Model Materials for Modern Nuclear Fuels. *Materials* **14** (2021). https://doi.org/10.3390/ma14206160

34 Murphy, G. L. *et al.* Deconvoluting Cr states in Cr-doped UO_2 nuclear fuels via bulk and single crystal spectroscopic studies. *Nat Commun* **14** (2023). https://doi.org/10.1038/s41467-023-38109-0

35 Murphy, G. L. *et al.* The role of redox and structure on grain growth in Mn-doped UO_2. *Communications Materials* **5**, 274 (2024). https://doi.org/10.1038/s43246-024-00714-x

36 Murphy, G. L. *et al.* Structural and chemical insights on the incorporation of americium into zircaloy-derived monoclinic zirconia. *Communications Chemistry* **9**, 50 (2025). https://doi.org/10.1038/s42004-025-01857-9

37 Shirokiy, D. *et al.* Speciation and Radiation Stability of Cr and *Ln* “Grey-Phases” within Cr-doped (*Ln*,U)O_2 Spent Fuel Model Materials. *Npj Mat Degrad* **10** (2026). https://doi.org/10.1038/s41529-026-00752-5

38 Ge, L., Subhash, G., Baney, R. H. & Tulenko, J. S. Influence of processing parameters on thermal conductivity of uranium dioxide pellets prepared by spark plasma sintering. *J Eur Ceram Soc* **34**, 1791-1801 (2014). https://doi.org/10.1016/j.jeurceramsoc.2014.01.018

39 Wangle, T., Tyrpekl, V., Cologna, M. & Somers, J. Simulated UO_2 fuel containing CsI by spark plasma sintering. *J Nucl Mater* **466**, 150-153 (2015). https://doi.org/10.1016/j.jnucmat.2015.07.030

40 Vinograd, V. L., Bukaemskiy, A. A., Modolo, G., Deissmann, G. & Bosbach, D. Thermodynamic and Structural Modelling of Non-Stoichiometric *Ln*-Doped UO_2 Solid Solutions *Ln* = {La, Pr, Nd, Gd}. *Front Chem* **9** (2021). https://doi.org/10.3389/fchem.2021.705024

41 Shannon, R. D. Revised Effective Ionic-Radii and Systematic Studies of Interatomic Distances in Halides and Chalcogenides. *Acta Crystallogr A* **32**, 751-767 (1976). https://doi.org/10.1107/S0567739476001551

42 Williams, H. R. *et al.* Metal matrix composite fuel for space radioisotope energy sources. *J Nucl Mater* **433**, 116-123 (2013). https://doi.org/10.1016/j.jnucmat.2012.09.030

43 Raiwa, M., Savina, M. R., Roberts, A. G., Shulaker, D. Z. & Isselhardt, B. H. Actinide Elemental Ratios of Spent Nuclear Fuel Samples by Resonance Ionization Mass Spectrometry. *J Am Soc Mass Spectr* **35**, 3233-3241 (2024). https://doi.org/10.1021/jasms.4c00371

44 Zhao, R. *et al.* A facile additive-free method for tunable fabrication of UO_2 and U_3O_8 nanoparticles in aqueous solution. *Crystengcomm* **16**, 2645-2651 (2014). https://doi.org/10.1039/c3ce42140f

45 Tyrpekl, V. *et al.* Implementation of a spark plasma sintering facility in a hermetic glovebox for compaction of toxic, radiotoxic, and air sensitive materials. *Rev Sci Instrum* **86** (2015). https://doi.org/10.1063/1.4913529

46 Carbol, P., Fors, P., Van Winckel, S. & Spahiu, K. Corrosion of irradiated MOX fuel in presence of dissolved H_2. *J Nucl Mater* **392**, 45-54 (2009). https://doi.org/10.1016/j.jnucmat.2009.03.044

47 Toby, B. H. & Von Dreele, R. B. GSAS-II: The genesis of a modern open-source all purpose crystallography software package. *J Appl Crystallogr* **46**, 544-549 (2013). https://doi.org/10.1107/S0021889813003531

48 Scheinost, A. C. *et al.* ROBL-II at ESRF: a synchrotron toolbox for actinide research. *Journal of Synchrotron Radiation* **28**, 333-349 (2021). https://doi.org/10.1107/S1600577520014265

49 Jacobson, N. S., Colle, J. Y., Stolyarova, V., Markus, T. & Nuta, I. Knudsen effusion mass spectrometry: Current and future approaches. *Rapid Communications in Mass Spectrometry* **38**, e9744 (2024). https://doi.org/10.1002/rcm.9744

50 Herrero, B. *et al.* Charge compensation mechanisms in Nd-doped UO_2 samples for stoichiometric and hypo-stoichiometric conditions: Lack of miscibility gap. *J Nucl Mater* **539** (2020). https://doi.org/10.1016/j.jnucmat.2020.152276

51 Schreinemachers, C. *et al.* Fabrication of Nd- and Ce-doped uranium dioxide microspheres via internal gelation. *J Nucl Mater* **535**, 152128 (2020). https://doi.org/10.1016/j.jnucmat.2020.152128

52 Tyrpekl, V. *et al.* On the Role of the Electrical Field in Spark Plasma Sintering of UO_{2+x}. *Sci Rep-Uk* **7**, 46625 (2017). https://doi.org/10.1038/srep46625

53 Lee, S. M., Knight, T. W., Voit, S. L. & Barabash, R. I. Lattice Parameter Behavior with Different Nd and O Concentrations in $(U_{1-y}Nd_y)O_{2\pm x}$ Solid Solution. *Nucl Technol* **193**, 287-296 (2016). https://doi.org/10.13182/nt14-136

54 Ohmichi, T., Fukushima, S., Maeda, A. & Watanabe, H. On the Relation between Lattice-Parameter and O/M Ratio for Uranium-Dioxide Trivalent Rare-Earth-Oxide Solid-Solution. *J Nucl Mater* **102**, 40-46 (1981). https://doi.org/10.1016/0022-3115(81)90544-4

55 Grønvold, F. High-Temperature X-Ray Study of Uranium Oxides in the UO_2-U_3O_8 Region. *J Inorg Nucl Chem* **1**, 357-370 (1955). https://doi.org/10.1016/0022-1902(55)80046-2

56 Cordfunke, E. H. P., Vanegmond, A. B. & Vanvoorst, G. Investigations on Cesium Uranates .1. Characterization of Phases in Cs-U-O System. *J Inorg Nucl Chem* **37**, 1433-1436 (1975). https://doi.org/10.1016/0022-1902(75)80785-8

57 Rochedy, M. *et al.* Comparative study of the I-UO_2 and Cs-UO_2 systems under conditions representative of irradiated fuel. *J Nucl Mater* **620**, 156348 (2025). https://doi.org/10.1016/j.jnucmat.2025.156348

58 Chen, X. A., Xue, H. P., Chang, X. N., Zang, H. G. & Xiao, W. Q. Hydrothermal synthesis and crystal structures of $Nd(IO_3)_3$ and $AI(IO_3)_3$. *J Alloy Compd* **398**, 173-177 (2005). https://doi.org/10.1016/j.jallcom.2005.01.050

59 Murphy, G. L. *et al.* The first actinide polyiodate: a complex multifunctional compound with promising X-ray luminescence properties and proton conductivity. *Chemical Communications* **57**, 496-499 (2021). https://doi.org/10.1039/d0cc06835g

60 Beneš, O., Konings, R. J. M. & Colle, J. Y. Determination of oxygen stoichiometry of oxide fuel during high temperature vapour pressure measurement. *J Nucl Mater* **462**, 182-190 (2015). https://doi.org/10.1016/j.jnucmat.2014.12.040

61 Götzmann, O. Thermochemical evaluation of PCI failures in LWR fuel pins. *J Nucl Mater* **107**, 185-195 (1982). https://doi.org/10.1016/0022-3115(82)90420-2

62 Liu, J. *et al.* Non-stoichiometric and Subnano-heterogeneous *Ln*-incorporated UO_2: its defect chemistry and thermal oxidation. *arXiv preprint arXiv:2412.03501* (2024). https://doi.org/10.48550/arXiv.2412.03501

63 Brandt, F. *et al.* The reactivity of Nd and Gd doped UO_2 in contact with H_2O_2 *In preparation* (2026).

64 Vinograd, V. L., Bukaemskiy, A. A., Deissmann, G. & Modolo, G. Thermodynamic model of the oxidation of *Ln*-doped UO_2. *Sci Rep-Uk* **13** (2023). https://doi.org/10.1038/s41598-023-42616-x

65 Vinograd, V. L. & Vauchy, R. A thermodynamic study of fluorite/bixbyite equilibria in the UO_2–$PuO_{1.5}$–PuO_2 system. *J Nucl Mater* **619**, 156244 (2026). https://doi.org/10.1016/j.jnucmat.2025.156244

66 Tessman, J. R., Kahn, A. H. & Shockley, W. Electronic Polarizabilities of Ions in Crystals. *Phys Rev* **92**, 890-895 (1953). https://doi.org/10.1103/PhysRev.92.890

Supplementary Files

This is a list of supplementary files associated with this preprint. Click to download.

- NdUO2CsISI.docx